Cement and Concrete Research 42 (2012) 440–446

Contents lists available at SciVerse ScienceDirect

Cement and Concrete Research

journal homepage: http://ees.elsevier.com/CEMCON/default.asp

Permeability and elastic modulus of cement paste as a function of curing temperature

John J. Valenza II *, Jeffrey J. Thomas

Schlumberger-Doll Research, One Hampshire St., Cambridge, MA 02139, USA

ARTICLE INFO

Article history:
Received 2 August 2011
Accepted 15 November 2011

Keywords:
Permeability (C)
Mechanical Properties (C)
Curing Temperature (A)
Characterization (B)

ABSTRACT

The permeability and elastic modulus of mature cement paste cured at temperatures between 8 °C and 60 °C were measured using a previously described beam bending method. The permeability increases by two orders of magnitude over this range, with most of the increase occurring when the curing temperature increases from 40 °C to 60 °C. The elastic modulus varies much less, decreasing by about 20% as the curing temperature increases from 20 °C to 60 °C. All specimens had very low permeability, $k<0.1$ nm^2, despite having relatively high porosity, $\phi \sim 40\%$. Concomitant investigations of the microstructure using small angle neutron scattering and thermoporometry indicate that the porosity is characterized by nanometric pores, and that the characteristic size of pores controlling transport increases with curing temperature. The variation of the microstructure with curing temperature is attributed to changes in the pore structure of the calcium–silicate–hydrate reaction product. Both the empirical Carmen–Kozeny, and modified Carmen–Kozeny permeability models suggest that the tortuosity is very high regardless of curing temperature, $\xi \sim 1000$.

1. Introduction

The hydration of portland cement results in the precipitation of product phases onto the surface of the unhydrated cement grains. These products grow into the capillary pore space, originally occupied by the mix water, decreasing the volume and connectivity of the intergranular porosity. The most important product phase for setting and hardening is the calcium silicate hydrate (C–S–H) gel, which contains internal, nanometer-scale gel pores that are an important aspect of its structure. Thus, as cement hydrates not only does the total porosity decrease, but the average pore size decreases by a few orders of magnitude. As a result, the permeability of cement paste is surprisingly low, typically lower than 1 nm^2. Low permeability prevents the ingress of dissolved species, and is therefore an important characteristic for cement durability.

The C–S–H gel does not form with a fixed structure, but rather the morphology, surface area, and internal porosity can vary depending on the location within the specimen and also on environmental conditions. Microscopy of hardened pastes generally shows that a porous outer product morphology of C–S–H forms outside the perimeter of the cement grains (LD C–S–H), while a denser inner product morphology fills the volume originally occupied by the cement grains (HD C–S–H) [1]. The Jennings colloid model [2] proposes that C–S–H in mature paste forms with two packing densities of the same fundamental 5 nm C–S–H particles, resulting in interparticle gel pores that are about 2 nm in size. This general picture is supported by a variety of experimental measurements including nanoindentation [3,4]. Hydrogen NMR relaxometry indicates that the pore system in cement hydrated at room temperature is bimodal, with characteristic pore sizes of ~1–2 nm and 10–30 nm [5–7].

Curing cement paste at moderately elevated temperatures results in microstructural differences that are apparent from microscopy [8]. At higher temperatures the hydration product layers around the cement grains appear denser, and the microstructure appears less uniform, with a greater number of large (capillary) pores. This has been attributed to the formation of C–S–H gel with a smaller volume of gel pores [3,9].

This work is motivated in part by inconsistent results regarding the effect of curing temperature on the transport properties of hardened cement paste. Goto and Roy [10] measured the permeability of cement pastes cured at 20 °C and 60 °C using the standard pressure gradient method, and found that at a given water to cement mass ratio (w/c) the permeability after curing at 60 °C was at least an order of magnitude higher. The authors attributed the variation in permeability to a variation in the pore size distribution. Detwiler et al. [11] measured the rate of chloride diffusion (a parameter that depends in part on the permeability) of cement pasted cured at 5, 20, and 50 °C and found a more modest increase of a factor of 2 between 20 and 50 °C, but little change between 5 and 20 °C. In contrast, Marsh et al. [12] found that the permeability of neat cement paste cured at 20, 35, 50, and 65 °C did not exhibit a strong dependence on curing temperature, although there is a large amount of scatter in their data.

Conventional techniques for measuring permeability, like those used in the studies noted above, are cumbersome, time consuming,

* Corresponding author. Tel.: +1 617 768 2346; fax: +1 617 768 2388.
E-mail address: jvalenza@slb.com (J.J. Valenza).

0008-8846/$ – see front matter © 2011 Elsevier Ltd. All rights reserved.
doi:10.1016/j.cemconres.2011.11.012

and markedly susceptible to experimental errors [13–15]. Therefore, the permeability measurement itself could be a major source of inconsistency. In the more recent past, the beam bending method, developed by Scherer [16,17], was applied to cement paste with good success [18–20]. This technique provides a consistent, convenient measure of the elastic and transport properties of a porous medium.

Here we revisit the effect of curing temperature on both the microstructure and properties of cement paste. The former is characterized by small angle neutron scattering (SANS) [3] and thermoporometry (TPM) [21], while the latter is characterized by beam bending. We utilize this information to provide insight into how the curing temperature affects the macroscopic properties via changes in the microstructure.

2. Experimental

2.1. Materials

All pastes were made with Type I OPC (Lafarge). For each batch, 900 g of cement was mixed with 405 g of water, giving w/c = 0.45. The paste was mixed by hand with a plastic spatula for 5 min and then poured into a plexiglas mold with four compartments, each with internal dimensions of 254 mm × 25 mm × 25 mm. The mold was tapped onto the counter for approximately 1 min to remove trapped air bubbles, and then sealed into a plastic container with a small amount of water at the bottom. For the pastes cured at 40 °C and 60 °C, the sealed mold was partially submerged in a circulating water bath. For the paste cured at 20 °C, the paste remained in the laboratory which was maintained at that temperature. The remaining batch was placed into a refrigerator which was maintained at 8 ± 1 °C. Pastes were demolded after 24 h (20, 40, 60 °C) or 48 h (8 °C) by disassembling the mold. The bars were then cured under lime water at the same temperature for an additional three months. After this time, all bars were stored at room temperature under the same saturated conditions until testing.

To form rectangular prismatic specimens for the beam bending experiments, the bars were cut lengthwise to thicknesses ranging from 3 mm to 7 mm using a water-lubricated diamond saw. Prior to the beam bending test, the specimens were pressurized at 3 MPa for 24 h while under lime water. This handling is necessary to ensure saturation of the pore system [18]. To determine the permeability and elastic modulus from the beam bending data it is necessary to measure the porosity (see Section 2.4). This parameter was inferred from the weight loss upon drying at 105 °C as measured on companion samples.

2.2. Small angle neutron scattering

The same cement paste specimens were analyzed using small angle neutron scattering (SANS). Thin (0.6 mm thick) specimens were cut from the rectangular bars using a water-lubricated wafering saw. After cutting the samples were stored and analyzed in the water-saturated state. The measurements were performed at the NIST Center for Neutron Research using the NIST/NSF NG3 30-m SANS instrument with a neutron wavelength of 0.8 nm. By varying the sample-to-detector distance, data for each specimen were obtained over a magnitude range of scattering vector of $0.02 < q < 3.0\ \mathrm{nm}^{-1}$, where $q = 4\pi\sin(\phi/2)/\lambda$, ϕ is the angle of scatter, and λ is the neutron wavelength. Scattering from hydrated cement paste in this q-range is dominated by the interface between the solid nanoscale C–S–H hydration product and the pore fluid, i.e. the gel pores. In general, the upper limit in q for obtaining data from hydrating cement is about $2\ \mathrm{nm}^{-1}$, due to the decrease in SANS intensity with increasing q.

For cement paste specimens it has previously been established that a Porod scattering regime exists at the highest accessible q values, where the scattering arises almost entirely from the nanoscale C–S–H gel. In the range of $1.4 < q < 2.0\ \mathrm{nm}^{-1}$ the scattering follows:

$$Int = \frac{C_P}{q^4} + BGD \tag{1}$$

where Int is the absolutely calibrated scattering intensity, C_P is the Porod constant, and BGD is incoherent scattering present as a flat (q-independent) background. The values of C_P and BGD are determined from a linear fit as shown in Fig. 1. The constant BGD value is subtracted from the scattering data to remove the flat background, while C_P is used to determine the specific surface area per unit specimen volume, S_T, according to:

$$S_T = \frac{C_P}{2\pi\Delta\rho^2} \tag{2}$$

where $\Delta\rho^2$, the neutron scattering contrast, is the square of the difference in the neutron scattering lengths of the phases generating the Porod scattering (solid C–S–H and water). The appropriate contrast for Eq. (2) was previously determined to be $9.74 \times 10^{28}\ \mathrm{m}^{-4}$ [22].

2.3. Thermoporometry

The pore systems of the cured cement pastes were also characterized using a cryogenic technique devised by Brun et al. [21] known as thermoporometry (TPM). This technique relies on the fact that a crystal confined in a small pore (i.e. <100 nm) melts at a lower temperature than a bulk crystal. The melting point depression is proportional to the curvature of the crystal/liquid interface, κ_{CL}, as described by the Gibbs–Thomson equation [23]:

$$\gamma_{CL}\kappa_{CL} = \int_T^{T_M} \Delta S_{fv} dT \tag{3}$$

where T is the melting temperature of the confined crystal, T_M is the bulk melting point, γ_{CL} is the crystal/liquid interfacial energy, and ΔS_{fv} is the entropy of fusion per unit volume of crystal. The curvature is governed by both the size, r_p, and geometry of the confining pore. For example, $\kappa_{CL} = 2/r_p$ for a hemispherical crystal/liquid interface, or $\kappa_{CL} = 1/r_p$ for a cylindrical interface.

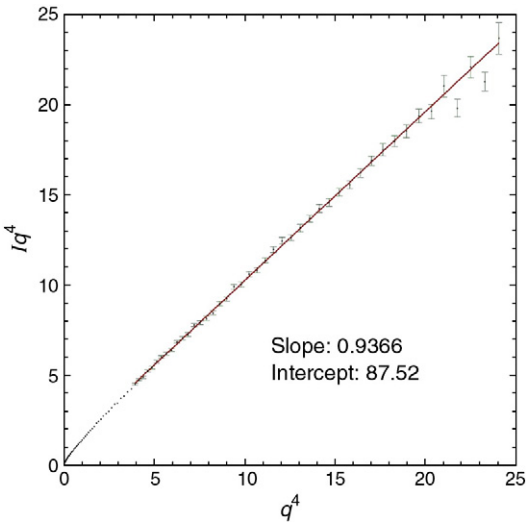

Fig. 1. Porod plot of the absolutely calibrated SANS data for cement paste hydrated at 20 °C. The solid line is a linear fit, for which the slope and intercept are given. The slope is the incoherent flat background scattering and the intercept is the Porod constant (see Eq. (1)).

TPM is performed with a differential scanning calorimeter (DSC), which monitors the heat flow during a phase transition as the temperature is changed. During a typical TPM experiment, the sample is first conditioned by exposing it to a very low temperature to freeze all of the pore liquid. Then, the temperature is increased to just below T_M, melting most of the pore liquid but leaving bulk crystals distributed throughout the system (e.g. on the surface or in large voids or pores). The analysis is then conducted on a second cooling ramp, as the sample is gradually refrozen. As the temperature is reduced the seed crystals grow and penetrate the fine microstructure with no nucleation barrier, obeying Eq. (3). The penetration of ice during a TPM experiment is analogous to mercury intrusion porosimetry (MIP).

The TPM experiments were performed on approximately 100 mg samples of coarsely ground cement paste. Initial freezing was at −60 °C, followed by melting up to −0.5 °C. The temperature was then slowly ramped down to −35 °C at −0.1 °C/min. The heat flow and temperature were logged throughout the experiment using software provided by the instrument manufacturer (TA Instruments).

2.4. Beam bending

A schematic of the beam bending experiment is shown in Fig. 2. The arrangement consists of simply supporting a slender beam of a homogeneous permeable medium in a bath of liquid with the same composition as the pore liquid. The measurement consists of monitoring the load, $W(t)$, after the beam is suddenly, symmetrically, deflected in three-point bending. When the beam is first bent, a pressure gradient forms in the pore liquid with compression above, and suction below the neutral axis. In response, fluid flows through the pores to alleviate these gradients, causing $W(t)$ to decrease with time. Both the permeability and the elastic modulus of the porous body can be determined by analyzing this time-dependent load relaxation.

Solutions for $W(t)$ were originally obtained for beams of circular or square cross section [16,17]. The theory was then extended to describe the load relaxation in isotropic and transversely isotropic beams of rectangular cross section [24]. The method was tested with porous Vycor® glass [25], and the measured permeability was consistent with that expected from the Carmen–Kozeny analysis [26] given the characteristic pore size and porosity of the glass.

In this study we used slender plates with a rectangular cross-section, for which the hydrodynamic load relaxation is estimated as [24]:

$$\frac{W(\theta)}{W(0)} = 1 - A + AS_1(\theta)S_2(\kappa\theta) \tag{4}$$

where A is the fraction of the load borne by the pore fluid:

$$A = \frac{\left(\frac{1-2\nu_P}{3}\right)\left(1-\frac{K_P}{K_S}\right)^2}{1-\frac{K_P}{K_S}+(1-\rho_S)\left(\frac{K_P}{K_L}-\frac{K_P}{K_S}\right)}. \tag{5}$$

In Eq. (5) ν is Poisson's ratio, K is the bulk modulus, and ρ_S is the volume fraction of solids ($\rho_S = 1-\phi$, where ϕ is the porosity). The subscripts P, S, and L indicate quantities that correspond to the porous body, the solid phase, and the liquid, respectively. In Eq. (4) the relaxation functions S_1 and S_2 represent relaxation along the thickness (a in Fig. 2) and the width (b in Fig. 2) of the beam, respectively:

$$S_1(\theta) = \sum_{n=1}^{\infty} \frac{6}{\pi^2 n^2} exp\left(-n^2\pi^2\theta\right) \tag{6}$$

and

$$S_2(\kappa\theta) = \sum_{m=1}^{\infty} \frac{8}{\pi^2(2m-1)^2} exp\left[\frac{-(2m-1)^2\pi^2}{4}\kappa\theta\right] \tag{7}$$

where $\kappa = a^2/b^2$ is the square of the aspect ratio of the cross section (Fig. 2), and $\theta = t/\tau_B$ is the reduced time. To analyze the experimental data we use the following approximations for $S_1(\theta)$ and $S_2(\kappa\theta)$ [24]:

$$S_1(\theta) \approx exp\left[-\left(\frac{6}{\sqrt{\pi}}\right)\left(\frac{\theta^{0.5}-\theta^{2.5}}{1-\theta^{0.551}}\right)\right] \tag{8}$$

and

$$S_2(\kappa\theta) \approx exp\left[-\left(\frac{2}{\sqrt{\pi}}\right)\left(\frac{\theta^{0.5}-\theta^{2.094}}{1-\theta^{0.670}}\right)\right]. \tag{9}$$

The hydrodynamic relaxation time, τ_B is given by:

$$\tau_B = \mu_B\left(\frac{\eta_L}{k}\right)\left(\frac{a^2}{K_P}\right) \tag{10}$$

where η_L is the viscosity of the liquid, k is the permeability, and μ_B is a material constant that modulates the diffusive relaxation time (i.e.: $\tau = (\eta_L a^2)/(kK_P)$ [27]) for concomitant strain in the pore liquid, and the solid phase:

$$\mu_B = \left(1-\frac{K_P}{K_S}\right)^2 + \frac{3(1-\rho_S)}{2(1+\nu_P)}\frac{K_P}{K_L} + \frac{3(\rho_S - K_P/K_S)}{2(1+\nu_P)}\frac{K_P}{K_S}. \tag{11}$$

The derivation of Eqs. (4)–(11) was presented in detail by Scherer [24] and the accuracy of the analysis for plate with rectangular cross-section was later verified by Valenza and Scherer [20].

Eq. (7) indicates that relaxation due to flow along the width of the beam (the larger dimension of the cross section) is diminished by reducing κ. It was previously shown in Ref. [24] that when $\kappa < 0.04$ the effect of flow along the width is negligible. With few exceptions, the dimensions of the cement paste plates used here are such that κ falls below this bound.

The beam bending apparatus is very similar to the one described in Ref. [25]. In general, the sample dimensions and imposed deflection are manipulated to allow τ_B to be accurately determined, and

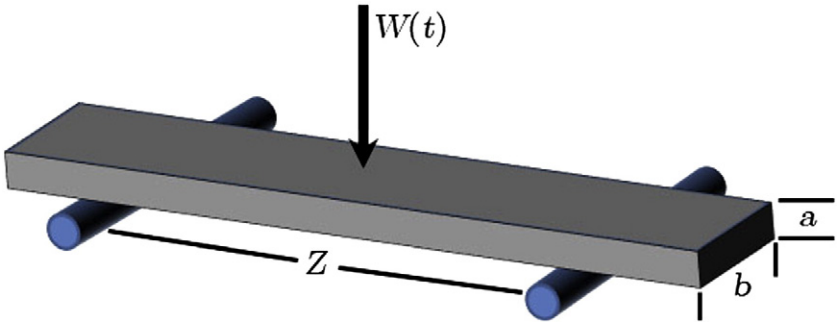

Fig. 2. Schematic of beam bending experiment.

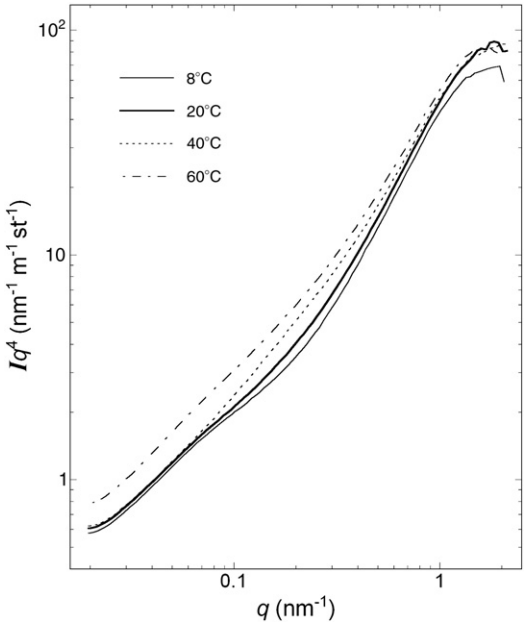

Fig. 3. SANS response of the cement paste specimens cured at different temperatures.

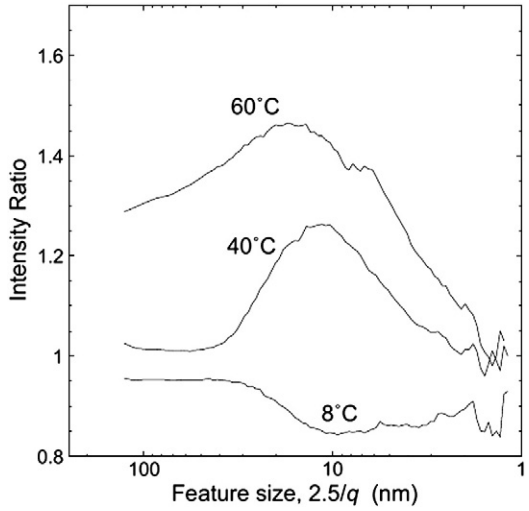

Fig. 4. SANS intensities at 8 °C, 40 °C, and 60 °C, each normalized to the intensity at 20 °C, plotted as a function of the feature size, R, from which the scattering arises. Pastes cured at higher temperatures generate more scattering from features on the order of 10 nm in size.

to ensure that the maximum stress is below 1 MPa. The latter bound is well below the tensile strength of hardened cement paste, ~3 MPa.

3. Results and discussion

3.1. SANS

Fig. 3 shows the SANS data for the pastes cured at different temperatures. These data are plotted in log–log format as Iq^4 vs. q, where I is the absolute-calibrated scattering intensity (with the flat background subtracted) at a given q. Plotting the data in this way enhances differences between related cement datasets [28]. These datasets show two distinct power–law regimes that have previously been interpreted as surface fractal scattering (at lower q) associated with the deposition of hydration product onto the hydrating cement particles, and volume fractal scattering associated with the fine nanoscale C–S–H structure [29–31].

Surface area values (Eq. (2), and Section 2.2) for the pastes are given in Table 1. The S_T values for curing temperatures between 20 °C and 60 °C are very similar, while the value for 8 °C is slightly lower, probably due to a lower amount of hydration at this temperature. This indicates that the amount of nanoporous C–S–H gel in these pastes is similar, particularly for those cured between 20 °C and 60 °C. Differences in the SANS response (Fig. 3) are therefore associated with differences in the nanostructure of the hydration products, such as differences in the arrangement and packing density of the fundamental C–S–H particles.

The SANS results in Fig. 3 indicate that samples cured at higher temperatures induce more scattered intensity at intermediate q values. For fractal systems such as cement paste, the linear size of objects that contribute most to the scattering at a given q is approximately $R = 2.5/q$ [32]. In Fig. 4, the ratios of the scattered intensities at 8, 40, and 60 °C to the intensity at 20 °C are plotted as a function of R. For samples cured at high temperatures, the relative scattering intensity increases the most at q-values corresponding to features greater than 10 nm in size. Coupled with the relatively consistent S_T values, this observation is interpreted as an increase in the size of pores through and around the nanoscale C–S–H gel. We believe this change is caused by an increase in the packing density of the C–S–H gel particles at higher temperatures, which causes the LD C–S–H phase (solid particles plus smallest gel pores) to fill the capillary pore space less efficiently, yielding a greater proportion of larger pores (e.g. 10–30 nm vs. 2 nm, Fig. 4).

Table 1
Specific surface areas determined from SANS.

Curing temp.	S_T (m^2/cm^3)
8 °C	111 (6)[a]
20 °C	137 (7)
40 °C	134 (7)
60 °C	137 (7)

[a] The numbers in parentheses are estimated standard deviations in least significant digits.

3.2. TPM

The results from the TPM experiments are shown in Fig. 5 where the data correspond to ice penetration during the second gradual cooling ramp. Each sample exhibits an initial abrupt increase in ice formation at an undercooling in the range of 2–3.5 °C. We interpret

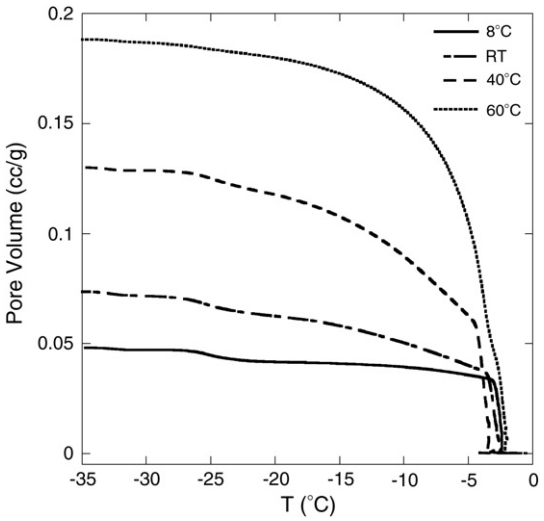

Fig. 5. TPM results for cement pastes cured at different temperatures. Cumulative frozen pore volume is plotted as a function of the temperature during the second freezing ramp. All pastes exhibit an initial abrupt increase in pore volume at undercoolings of 2 − 3.5 °C, which corresponds to a pore size of $r_p = 19$–33 nm. The porosity accessible through pores of this size increases with curing temperature.

this event as ice, present from the initial freezing step, penetrating the pore network. This interpretation is supported by the fact that in all cases heterogeneous ice formation is observed at a significantly lower temperature ($\Delta T = 13-16$ °C) during the initial freezing step. Similar to the intrusion of mercury during MIP, we assume that the ice penetrates the network with a hemispherical crystal/liquid interface, so the size of the pores (in nm) governing penetration is given by [21,33]:

$$r_P(\text{nm}) = \frac{64.67}{\Delta T} + 0.97. \tag{12}$$

Eq. (12) accounts for the temperature dependence of γ_{CL}, and the entropy of fusion of water [21,33]. In addition, this expression accounts for an aqueous liquid-like film that separates the confined ice from the pore wall [21,33]. Brun et al. [21] determined the film thickness to be ≈0.8 nm by comparing TPM results to MIP. Through a similar comparison of TPM to nitrogen adsorption performed on porous glass, Sun and Scherer [33] found a slightly larger value for the film thickness (≈1 nm) when water is replaced by an aqueous solution saturated with CaO. In Eq. (12) we utilize the larger film thickness, which we interpret to be representative of cementitious systems.

Given the data in Fig. 5, Eq. (12) indicates that ice penetrates the pore network through pores characterized by $r_P \approx 20$–30 nm. As noted earlier, NMR relaxometry indicates that cement paste has a bimodal nanopore system characterized by sizes of 1–2 nm and 10–30 nm. However, based on the above discussion the pores in the smaller size range are not accessible to ice due to the unfrozen liquid film. Therefore, we interpret the low temperature asymptote in Fig. 5 as the fraction of the porosity accessible from the larger (≈20–30 nm) pores in the bimodal distribution. From Fig. 5 it is clear that more of the porosity is accessible through the larger mesopores as the curing temperature increases; This result is consistent with the SANS data (Fig. 4), which show an increase in intensity associated with features of this size.

3.3. Beam bending

Typical results from a beam bending experiment are shown in Fig. 6. The plot shows the load (normalized to the initial load) versus time. There are two distinct regimes of load relaxation separated by an inflection centered at t~300 s. Previous experience indicates that the location of this inflection is roughly given by τ_B/C, where $C \approx 3-5$. The relaxation at early time is hydrodynamic, while relaxation at longer time is viscoelastic. It was previously demonstrated [17] that the relaxation due to the two mechanisms is clearly distinguishable as long as τ_B is at least 100 times smaller than the characteristic viscoelastic relaxation time. In this case, the data can be fit by a product of two relaxation functions:

$$\frac{W(t)}{W(0)} = R_{HD}(t)\Psi_{VE}(t) \tag{13}$$

where $R_{HD}(t)$ is the hydrodynamic relaxation function given by Eq. (2) and $\Psi_{VE}(t)$ is a viscoelastic relaxation function. The latter is represented by one of two expressions, depending on the amount of load relaxation that occurs. If the load relaxation is greater than 20% then we use a combination of stretched exponential functions that was previously shown to be reproducibly representative of cement paste [19,20]. Otherwise we use a single stretched exponential function to represent $\Psi_{VE}(t)$. In both cases there are two additional fitting parameters; two relaxation times in the former case, or a relaxation time and an exponent in the latter case. These parameters are adjusted to account for the relaxation that occurs after the end of hydrodynamic relaxation (Fig. 6). In all cases, the viscoelastic relaxation times are at least 3 orders of magnitude greater than that for hydrodynamic relaxation, and the related exponents are less than unity. So the relaxation processes occur on significantly different time scales.

As discussed extensively elsewhere [17,24], the values of A and τ_B that yield the best fit to the data corresponding to hydrodynamic relaxation are used to determine the permeability (see Eq. (10)), and the elastic modulus of the cement paste:

$$E_P = \frac{W(0)(1-A)Z^3}{48\Delta M} \tag{14}$$

where Δ is the measured deflection, Z is the span (Fig. 2), and $M = (ba^3)/12$ is the moment of inertia. To complete the analysis it is necessary only to assume a value for $\nu_P = 0.25$ and the relationship between the bulk moduli corresponding to the porous medium, which we set to $K_S/K_P = \rho_S^2$ based on previous experience [18]. It was previously shown that the permeability is not markedly dependent on these assumptions [18].

Fitted values of the elastic modulus for pastes cured at temperatures in the range of 8–60 °C are shown in Fig. 7. The values of E_P do not have a large variation with curing temperature, as expected

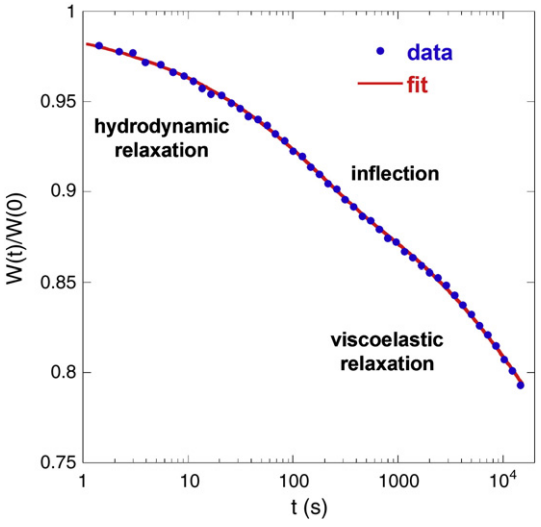

Fig. 6. Results from a typical beam bending experiment on a sample cured at 20 °C. The open circles are the data (normalized load vs. time) and the solid line is the fit.

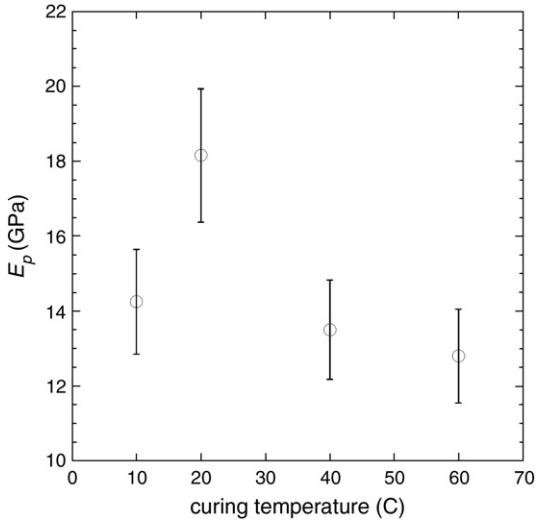

Fig. 7. Elastic modulus of cement paste specimens as a function of curing temperature, obtained from beam bending measurements. Error bars represent the average standard deviation as a percentage of the mean value at each curing temperature.

based on the relatively consistent porosity, but some trends are apparent.

The highest modulus is obtained for 20 °C curing, and there is a decrease in modulus with increasing curing temperature above 20 °C. The modulus value at 20 °C is in excellent agreement with previous measurements using beam bending by Vichit-Vadikan et al. [18], and in that same paper the authors reported good agreement with modulus values calculated from ultrasonic pulse velocity. Kim et al. [34] measured the compressive strength and modulus of cement paste cured at different temperatures, reporting the chord elastic modulus value from compression testing according to ASTM C469. Their modulus values are about 50% higher than those reported from beam bending (i.e. 30 GPa vs. 20 GPa for mature paste with w/c = 0.4). A variation of this magnitude between very different techniques is not surprising given that cement paste is a nonlinear inelastic material [35].

In agreement with the present results, Kim et al. [34] found that the elastic modulus of 28 day old specimens decreased with increasing curing temperature, as did the compressive strength. In fact, well established empirical relationships show that the compressive strength and elastic modulus of cement paste and concrete vary together under a range of conditions. The decrease in both of these parameters with increasing curing temperature can be attributed to an increase in capillary porosity [36] due to less efficient filling of the capillary pore space by hydration product.

Fitted values of the permeability are plotted in Fig. 8. The permeability increases by a factor of 2 between 20 °C and 40 °C, and increases by nearly 2 orders of magnitude between 20 ° and 60 °C. The very low permeability value obtained at 8 °C and 20 °C (about 0.001 nm^2) is in good agreement with previous beam bending measurements of mature pastes made with a similar w/c [18]. On the other hand, the permeability of the 60 °C specimen (0.1 nm^2) is similar to previous results [18] for an immature (about 3 d old) paste made with w/c = 0.6.

3.4. General discussion—relating permeability to microstructure

The measured permeability of cement paste is extremely low, particularly in view of its rather high total porosity (about 0.4 for the samples measured here). In comparison, porous rocks tend to have permeabilities that are several orders of magnitude higher, despite having lower porosities. The most widely used relationship for the permeability of a porous material is the Carmen–Kozeny equation [26]:

$$k = \frac{\phi r_P^2}{\xi} \tag{15}$$

where r_P is the size of pores controlling transport in the porous medium, and ξ is the Kozeny constant, also known as the tortuosity.

For random porous materials, r_P is often estimated by calculating the hydraulic radius r_H, defined as the pore volume divided by the wetted area. In the present case we have $r_H = \phi/S_T$, which yields $r_H \approx 3$ nm for all curing temperatures. In fact, C–S–H gel is not random, but has internal gel pores with a smallest characteristic size of about 2 nm [2,6], which is nonetheless reasonably close to the calculated r_H value. Using a value of 2 nm in Eq. (15) with the porosity and measured permeability for the samples cured at ambient temperature implies a tortuosity of $\xi \approx 2000$. This is in poor agreement with the calculated values of ξ = 3–5 for various model porous media with $\phi = 0.4$ [37]. To bring the inferred value for ξ into agreement with that for model porous media it would be necessary to assume that r_P is more than an order of magnitude smaller, which is unphysical as this would be smaller than a single water molecule.

An alternative to the Carmen–Kozeny equation was proposed by Avellaneda and Torquato [38]:

$$k = \frac{L^2}{8F} \tag{16}$$

where L is a length parameter that is the product of the kinematic viscosity and a weighted sum over the viscous relaxation times, and F is the formation factor, defined as the ratio of the electrical conductivity or diffusivity of the pore liquid to that of the corresponding saturated porous medium. In Eq. (16) the formation factor plays a similar role as the tortuosity in Eq. (15) in defining how strongly the geometry of the pore system impedes transport. However, unlike ξ, F is much simpler to measure directly. For cement paste, a hydration model was used to estimate a value of $F = 400$ from diffusivity data [39], and a value of $F = 230$ was calculated [40] based on the same microstructural model (e.g. gel consisting of 5 nm building blocks) that suggests $r_P = 2$ nm [2]. These values are in agreement with direct measurements on portland cement mortars using impedance spectroscopy, for which $F = 300$ for w/c = 0.4 and 28 d of hydration [41]. Utilizing the latter measured values for $F \approx 300$, and $k = 0.001$ nm^2 in Eq. (16), we find $L = 1.5$ nm, which is remarkably close to the gel pore size. This agreement supports a general interpretation that the controlling pore size for transport is on the order of 2 nm in these specimens but some aspect of the microstructure greatly hinders the dissipation of gradients in chemical potential.

Regarding the cement paste cured at 60 °C, the SANS data indicates that curing at 60 °C yields an increase in features that are greater than 10 nm, while the TPM data indicates that ice penetration, and thus transport, is governed by ≈20 nm pores. From Fig. 5 we see that the proportion of the porosity accessible from 20 nm pores increases by a factor of 2.7 over the range of curing temperatures investigated here. In particular, for the paste cured at 60 °C the porosity accessible through these pores comprises nearly 75% of the total porosity. Therefore, it seems reasonable to assume that transport is controlled by these larger (≈20 nm) pores in the paste cured at 60 °C, rather than the fundamental 2 nm gel pores. Eqs. (15) and (16) both indicate that a one order of magnitude increase in the characteristic pore size should result in an increase in permeability of two orders of magnitude, which is exactly the increase we observe (see Fig. 8). It is important to note that this agreement suggests that even in the case of higher curing temperature the microstructure severely limits the dissipation of gradients in chemical potential.

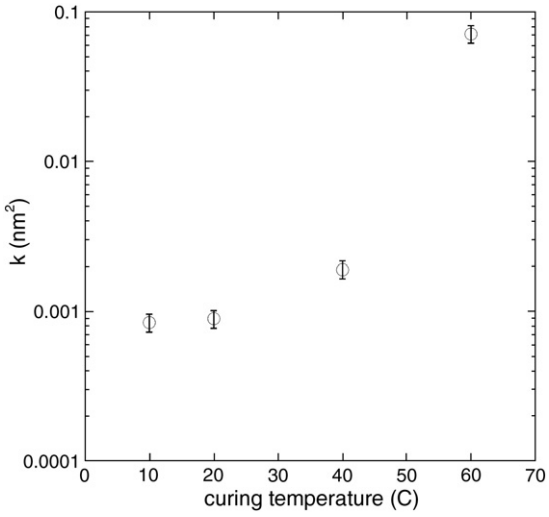

Fig. 8. Permeability of cement paste specimens as a function of curing temperature, obtained from beam bending measurements. Error bars represent the average standard deviation as a percentage of the mean value at each curing temperature.

4. Conclusions

Cement paste specimens cured at various temperatures in the range of $10-60\,^{\circ}C$ were characterized by beam bending to determine the permeability and elastic modulus, while SANS and TPM were used to characterize the microstructure. The permeability increases by two orders of magnitude over this curing temperature range, with most of the increase occurring when the curing temperature increases from 40 °C to 60 °C. The elastic modulus varies much less, decreasing by about 20% as the curing temperature increases from 20 °C to 60 °C. All specimens had very low permeability, $k < 0.1\,nm^2$, despite having relatively high total porosity, $\phi \sim 40\%$. SANS indicates that increasing the curing temperature from 20 °C to 60 °C yields a substantial increase in pores characterized by a size greater than 10 nm, which is an order of magnitude greater than the characteristic pore size in the gel. TPM shows that the amount of porosity accessible through ~20 nm pores increases by a factor of 3 as the curing temperature increases. Accordingly, the permeability of samples cured at high temperature is 2 orders of magnitude greater than the samples cured under ambient conditions where it is likely that transport is controlled by ≈ 2 nm gel pores. This observation is consistent with the implications of the Carmen–Kozeny model for permeability. Finally, our results suggest that flow in cementitious systems follows a highly convoluted path, regardless of the curing conditions. Altogether we interpret these results to indicate that fluid flow in hardened cement paste is governed by the morphology of the C–S–H gel on the scale of nm.

Acknowledgments

The authors would like to thank D. Johnson for several insightful discussions regarding the manuscript, and L. McGowan for cutting the beam bending plates. We also thank G. Scherer for providing the software to analyze the beam bending data.

References

[1] H.F.W. Taylor, Cement Chemistry, Thomas Telford, London, 1997.
[2] H.M. Jennings, A model for the microstructure of calcium silicate hydrate in cement paste, Cem. Concr. Res. 30 (2000) 101–116.
[3] H.M. Jennings, J.J. Thomas, J.S. Gevrenov, G. Constantinides, F.-J. Ulm, A multi-technique investigation of the nanoporosity of cement paste, Cem. Concr. Res. 37 (2007) 329–336.
[4] G. Constantinides, F.-J. Ulm, The nanogranular nature of C–S–H, J. Mech. Phys. Solids 55 (2007) 64–90.
[5] W. Halperin, J. Jehng, Y. Song, Application of spin–spin relaxation to measurement of surface area and pore size distributions in a hydrating cement paste, Magn. Reson. Imaging 12 (2) (1994) 169–173.
[6] L. Monteilhet, J.-P. Korb, J. Mitchell, P. McDonald, Observation of exchange of micropore water in cement pastes by two-dimensional t_2-t_2 nuclear magnetic resonance relaxometry, Phys. Rev. E 74 (2006) 061404.
[7] P. McDonald, V. Rodin, A. Valori, Characterisation of intra-and inter-C–S–H gel pore water in white cement based on an analysis of NMR signal amplitudes as a function of water content, Cem. Concr. Res. 40 (2010) 1656–1653.
[8] K.O. Kjellson, R.J. Detwiler, O.E. Gjorv, Pore structure of plain cement pastes hydrated at different temperatures, Cem. Concr. Res. 20 (1990) 927–933.
[9] A. Bentur, R.L. Berger, J.H. Kung, N.B. Milestone, J.F. Young, Structural properties of calcium silicate pastes: II, effect of curing temperature, J. Am. Ceram. Soc. 62 (1979) 362–366.
[10] S. Goto, D.M. Roy, The effect of w/c ratio and curing temperature on the permeability of hardened cement paste, Cem. Concr. Res. 11 (1981) 575–579.
[11] R.J. Detwiler, K.O. Kjellson, O.E. Gjorv, Resistance to chloride intrusion of concrete cured at different temperatures, ACI Mater. J. (Jan–Feb 1991) 19–24.
[12] B.K. Marsh, R.L. Day, D.G. Bonner, Pore structure characteristics affecting the permeability of cement paste containing fly ash, Cem. Concr. Res. 15 (1985) 1027–1038.
[13] T.C. Powers, E.A. Copeland, J.C. Hayes, H.M. Mann, Permeability of portland cement paste, J. Am. Concr. Inst. 51 (1954) 285.
[14] A.S. El-Dieb, R.D. Hooton, Water permeability measurement of high performance concrete using a high pressure triaxial cell, Cem. Concr. Res. 25 (6) (1995) 1199–1208.
[15] R.D. Hooton, A.S. El-Dieb, Evaluation of water permeability of high performance concrete, in: K. Sakai, N. Banthia, O.E. Gjørv (Eds.), Proceedings of International Conference on Concrete under Severe Conditions, Sapporo, Japan, Aug. 2–4 1995, Vol. 1, FN Spon, New York, 1995, pp. 423–432.
[16] G.W. Scherer, Bending of gel beams: method of characterizing mechanical properties and permeability, J. Non-Cryst. Solids 142 (1992) 18–35.
[17] G.W. Scherer, Measuring permeability of rigid materials by a beam bending method: I, theory, J. Am. Ceram. Soc. 83 (9) (2000) 2231–2239.
[18] W. Vichit-Vadakan, G.W. Scherer, Measuring permeability of rigid materials by a beam-bending method: III, cement paste, J. Am. Ceram. Soc. 85 (2002) 1537–1544.
[19] W. Vichit-Vadakan, G.W. Scherer, Measuring permeability and stress relaxation of young cement paste by beam-bending, Cem. Concr. Res. 33 (2003) 1925–1932.
[20] J.J. Valenza II, G.W. Scherer, Measuring permeability of rigid materials by a beam-bending method: V, isotropic rectangular plates of cement paste, J. Am. Ceram. Soc. 87 (2004) 1927–1931.
[21] M. Brun, A. Lallemand, J.F. Quinson, C. Eyraud, A new method for the simultaneous determination of the size and shape of pores: the thermoporometry, Thermochim. Acta 21 (1977) 59–88.
[22] A.J. Allen, J.J. Thomas, H.M. Jennings, Composition and density of nanoscale calcium–silicate–hydrate in cement, Nat. Mater. 6 (2007) 311–316.
[23] R. Defay, I. Prigogine, Surface Tension and Adsorption, John Wiley and Sons Inc., New York, New York, 1966.
[24] G.W. Scherer, Measuring permeability of rigid materials by a beam-bending method: IV, transversely isotropic material, J. Am. Ceram. Soc. 87 (8) (2003) 151724.
[25] W. Vichit-Vadakan, G.W. Scherer, Measuring permeability of rigid materials by a beam-bending method: II, porous Vycor, J. Am. Ceram. Soc. 83 (9) (2000) 2240–2245.
[26] P.C. Carman, Flow of Gases through Porous Media, Academic Press, 1956.
[27] H.S. Carslaw, J.C. Jaeger, Conduction of Heat in Solids, 2nd Edition Clarendon Press, Oxford, England, 1959.
[28] A.J. Allen, J.J. Thomas, Analysis of C–S–H gel and cement paste by small-angle neutron scattering, Cem. Concr. Res. 37 (2007) 319–324.
[29] A.J. Allen, R.C. Oberthur, D. Pearson, P. Schofield, C.R. Wilding, Development of the fine porosity and gel structure of hydrating cement systems, Philos. Mag. B 56 (1987) 263–268.
[30] J.J. Thomas, A.J. Allen, H.M. Jennings, Structural changes to the calcium silicate hydrate gel phase of hydrated cement with age and on drying and resaturation, J. Am. Ceram. Soc. 91 (2008) 3362–3369.
[31] J.J. Thomas, A.J. Allen, H.M. Jennings, Hydration kinetics and microstructure development of normal and $CaCl_2$-accelerated tricalcium silicate (C_3S) pastes, J. Phys. Chem. C 113 (2009) 19836–19844.
[32] A.P. Radlinski, C.J. Boreham, P. Lindner, O.P. Randl, G.D. Wignall, J.M. Hope, Small angle neutron scattering signature of oil generation in artifically and naturally matured hydrocarbon source rocks, Org. Geochem. 31 (2000) 1–14.
[33] Z. Sun, G.W. Scherer, Pore size and shape in mortar by thermoporometry, Cem. Concr. Res. 40 (2010) 740–751.
[34] J.K.J.K. Kim, S.H. Han, Y.C. Song, Effect of temperature and aging on the mechanical properties of concrete part I. Experimental results, Cem. Concr. Res. 32 (2002) 1087–1094.
[35] S. Mindess, J.F. Young, Concrete, Prentice-Hall, Englewood Cliffs, NJ, 1981.
[36] G.J. Verbeck, R.H. Helmuth, Structure and physical properties of cement pastes, Proceeding of the 5th International Symposium on the Chemistry of Cement, vol. 3, 1968, pp. 1–32, Tokyo, Japan.
[37] J. Happel, H. Brenner, Low Reynolds Number Hydrodynamics, Martinus Nijhoff, The Hague, 1983.
[38] M. Avellaneda, S. Torquato, Rigorous link between fluid permeability, electrical conductivity, and relaxation times for transport in porous media, Phys. Fluids A 3 (1991) 2529–2540.
[39] E.J. Garboczi, D.P. Bentz, Computer simulations of the diffusivity of cement based materials, J. Mater. Sci. 27 (1992) 2083–2092.
[40] D.P. Bentz, O.M. Jensen, A.M. Coats, F.P. Glasser, Influence of silica fume on diffusivity in cement-based materials I. experimental and computer modeling studies on cement pastes, Cem. Concr. Res. 30 (2000) 953–962.
[41] P. Tumidajski, A. Schumacher, S. Perron, P. Gu, J. Beaudoin, On the relationship between porosity and electrical resistivity in cementitious systems, Cem. Concr. Res. 26 (4) (1996) 539–544.